Structure

Resource

Trace_y: Software algorithms for structural analysis of individual helical filaments by three-dimensional contact point reconstruction atomic force microscopy

Graphical abstract

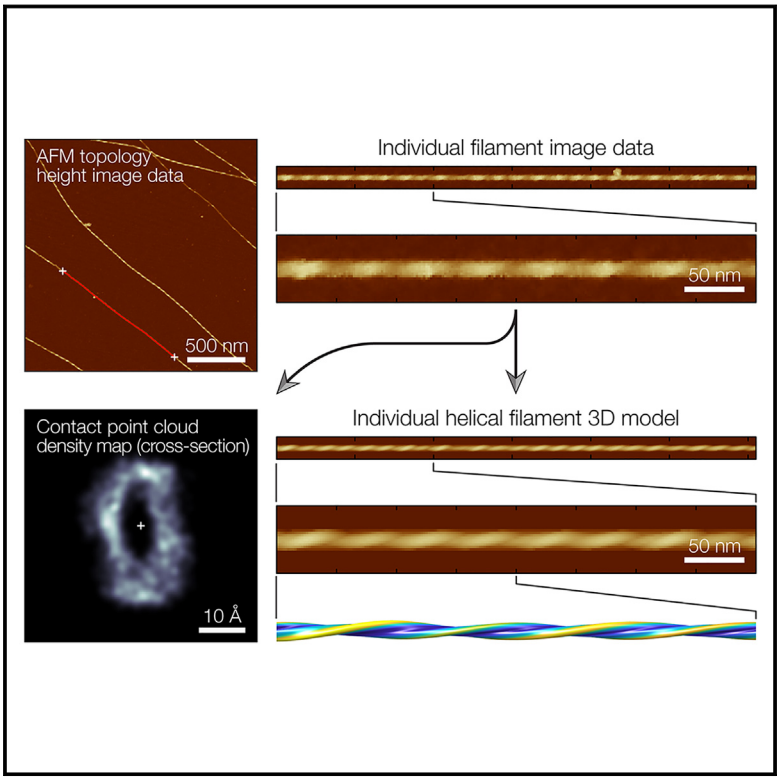

Authors

Wei-Feng Xue

Correspondence

w.f.xue@kent.ac.uk

In brief

Xue presents an open-source software designed to reconstruct the 3D surface envelopes of individual helical filament structures from topographical AFM height images. The reported algorithms enable the reconstruction of 3D information in AFM height images as tip-sample contact point clouds, thereby facilitating the use of AFM in integrative structural biology.

Highlights

- High signal-to-noise AFM images allow analysis of individual molecules without averaging
- 3D information is encoded in AFM height images as tip-sample contact point clouds
- Trace_y allows reconstruction of individual 3D filament structures from AFM images
- Individual particle structural analysis resolves polymorphous amyloid populations

Xue, 2025, Structure *33*, 363–371
February 6, 2025
https://doi.org/10.1016/j.str.2024.11.007

CellPress

Structure

CellPress
OPEN ACCESS

Resource

Trace_y: Software algorithms for structural analysis of individual helical filaments by three-dimensional contact point reconstruction atomic force microscopy

Wei-Feng Xue[1,2,*]
[1]School of Biosciences, Division of Natural Sciences, University of Kent, Canterbury CT2 7NJ, UK
[2]Lead contact
*Correspondence: w.f.xue@kent.ac.uk
https://doi.org/10.1016/j.str.2024.11.007

SUMMARY

Atomic force microscopy (AFM) is a powerful and increasingly accessible technology that has a wide range of bio-imaging applications. AFM is capable of producing detailed three-dimensional topographical images with high signal-to-noise ratio, which enables the structural features of individual molecules to be studied without the need for ensemble averaging. Here, a software tool Trace_y, designed to reconstruct the three-dimensional surface envelopes of individual helical filament structures from topographical AFM images, is presented. Workflow using Trace_y is demonstrated on the structural analysis of individual helical amyloid protein fibrils where the assembly mechanism of heterogeneous, complex and diverse fibril populations due to structural polymorphism is not understood. The algorithms presented here allow structural information encoded in topographical AFM height images to be extracted and understood as three-dimensional (3D) contact point clouds. This approach will facilitate the use of AFM in structural biology to understand molecular structures and behaviors at individual molecule level.

INTRODUCTION

Atomic force microscopy (AFM) is a powerful multimodal technique with imaging applications ranging from arrays of living cells to single molecules.[1] AFM is an increasingly accessible method that has been used to study molecular dynamics[2] and molecular responses to force.[3] It is also used for nanoscale imaging of biological molecules and structures in air or in liquid.[4–6]) AFM topographical imaging operates by sensing the physical contact between the probe, typically consisting of a sharp conical tip attached to a cantilever, and the specimen surface, to generate a three-dimensional (3D) height map of the sample surface.[7] While the imaging resolution of AFM is limited by the physical size of the AFM probe tip, molecular images acquired using AFM operating in non-contact mode with chemically functionalized probe tips is capable of reaching atomic resolution on samples of small planar molecules.[8] Imaging resolution using unmodified probe tips can also be enhanced to sub-nanometers through recent image analysis advances.[9] For structural biology applications, AFM offers several capabilities complementary to techniques, such as cryogenic electron microscopy (cryo-EM), X-ray crystallography, and nuclear magnetic resonance spectroscopy. These include the ability of imaging in ambient conditions and in liquid environment, allowing imaging of biological samples such as live cells in a close to native environment.[10–12] A key, sometimes overlooked, capability of AFM is that topographical images acquired by AFM can achieve a high signal-to-noise ratio, which enables structural features of individual molecules to be studied without the need for ensemble averaging.[13,14] This means that relevant structural information can be gained potentially from a single observation of a molecule on a single image. Therefore, this capability could offer new, exciting opportunities in elucidating rare molecular structures in complex, heterogeneous samples, and offer new information in the cases where the heterogeneity of molecular populations or the structural variations between individual molecules hold important biological relevance.

Amyloid fibrils represent a group of filamentous protein structures where the heterogeneity of the complex and mixed amyloid populations as well as the structural variations between the individual fibrils or even within individual fibrils hold relevant information regarding their biological impact.[15] Amyloid fibrils are typically ordered helical nano-structures around 10 nm wide and between few nm to several microns long. They are assembled from monomeric proteins or peptide precursors. Some amyloid structures are associated with devastating neurodegenerative disorders including Alzheimer's and Parkinson's diseases.[16–20] In contrast, some amyloid fibrils have been identified to fulfill essential biological functions, providing scaffolding, adhesion and protection for organisms from bacteria to fungi, and more recently discovered to provide regulatory control of memory[21] and for viral infection.[22] The formation of these functional amyloid fibrils is assumed to be tightly controlled. In contrast, the assembly of pathologically associated amyloid, even from a single type

of precursor, can result in highly heterogeneous molecular mixtures, as well as a spectrum of different individual filament structures called polymorphs. Thus, it is clear that amyloid structural polymorphism is common for disease associated amyloid and this polymorphism phenomenon has been suggested to be a property differentiating disease associated amyloid from functional ones.[15] AFM imaging has previously been used to characterize the morphological features of individual fibrils in a sample[13,23–26] and the size distributions of amyloid populations.[27–31] Recent advances in cryo-EM and solid-state nuclear magnetic resonance spectroscopy (ssNMR) have provided atomic-detailed structures showing multiple polymorphic forms for fibrils formed of identical precursors.[15] However, to resolve the extent of the polymorphic diversity and the roles polymorphs play in biology, one must be able to determine the structures of individual amyloid fibril particles,[32] and monitor their individual interactions in a complex and heterogeneous population to sufficient detail so that the diverse amyloid assembly landscapes, their polymorphic extents and biological properties linked to the heterogeneous populations can be mapped.

Here, an open-source image analysis software Trace_y (available at https://github.com/wfxue/Trace_y), featuring a collection of algorithms for 3D contact point reconstruction (CPR)[14] and structural analysis of individual helical filaments, is presented. The individual filament structural analysis workflow using Trace_y is demonstrated here on the analysis of helical amyloid protein fibrils formed from the 42 residues long amyloid β 1–42 peptide ($A\beta_{42}$) associated with Alzheimer's disease, where heterogeneous, complex and diverse fibril populations can assemble from a single monomer amino acid sequence in the same sample due to structural polymorphism.[33–35] Individual filament level structural analysis approach through 3D CPR-AFM, recently developed to utilize the high signal-to-noise topographical imaging capability of AFM,[13,14,35] has the potential to tackle the challenges presented by the structural analysis of complex and heterogeneous samples such as polymorphous amyloid fibrils.[36] The Trace_y software and the workflow for individual filament structural analysis presented here also demonstrate that the three-dimensional information encoded in AFM height images can be understood as 3D point clouds, which is a type of spatial information that could be integrated with other structural analysis methodologies.[37]

RESULTS

Overview of the Trace_y workflow and its algorithms

The purpose of the workflow presented here is to recover the 3D structural information of individually observed helical filaments encoded in topographical AFM height images. Figure 1 shows an overview of the workflow with a flowchart highlighting the key steps and the algorithms in the workflow with the example application to an individual fibril formed from the human $A\beta_{42}$ sequence.[35] The input for the workflow is an AFM height image where each pixel in the image contains the information of its x/y coordinate in the image lattice as well as the pixel value representing the recorded z coordinate of AFM probe tip when intermittent contact between the tip and the molecular surface of the sample was detected. Due to the physics behind AFM, topographical height images have high vertical (z axis) signal-to-noise ratio, with the noise typically in the order of sub-Ångströms range on current commercial instruments. One challenge of 3D structural reconstruction using AFM height image is that the recorded x, y, and z coordinates of the tip are not the actual tip-sample contact points,[14,38] which are not known. This issue is commonly referred to as the tip-sample convolution artifact. An important step in the workflow, therefore, is to deconvolute the image to recover the actual tip-sample contact points. Once the coordinates for tip-sample contact points are recovered, full 3D surface envelopes can be rendered for structures with helical symmetry, despite that only the top surface of the sample is accessible to the AFM tip, because structural information on the whole of a helical surface can be gained from a single direction of observation perpendicular to its helical axis due to their periodic twist around the helical axis. This requires the knowledge on the location of the helical axis, the handedness of the twist, and the pitch of the helical structure, all of which can be gained or estimated from the height images (Figures 1C–1E). The output of the workflow is a 3D contact point cloud of the surface of the helical filament, which can be further visualized as a 3D surface envelope model of the filament structure. The algorithms performing the key steps of the Trace_y workflow are explained in the following sections and exemplified on a fibril formed from recombinant human $A\beta_{42}$ (Figures 1B and 1C).

Individual filament tracing and estimation of the helical axis

A semi-automatic fibril tracing algorithm was developed to allow the user to select and to trace segments of individual filaments observed on AFM height images. Since the central contour line of a filament appearing in a height image typically corresponds to the projection of the filament's helical axis on the x/y plane, an accurate estimate of the central contour line of the selected filament is needed. Therefore, a curved Gaussian wall[39] model (Equation 1, STAR Methods) was used and fit by least-squares method to regions of the height image (image squares with edges twice the span of filament's apparent width) cropped along the coarse user-selected contours of the filament (Figure 2). This approach allows the x/y coordinates of points on the central contour line of the filament to be determined with sub-pixel accuracy because the coordinates are estimated using information from the entirety of the local features rather than few individual pixels. The z coordinate of the filament helical axis was subsequently estimated as half of the average peak height (for example, the peaks values at locations marked with triangles in Figure 1D). This simple estimate assumed a rigid fibril that rests on the support surface without substantial deformation during deposition and by the peak probing force during imaging.

3D contact point reconstruction by image deconvolution

The 3D coordinates of tip-sample contact points were next reconstructed by modeling rigid-body interactions between the AFM probe tip and the sample filament using the image deconvolution strategy as previously described.[14] Briefly, the tip geometry and approximate magnitude of image dilation due to tip-filament convolution was first estimated. A rounded cone tip model made by the rotation of the half cross-section described by Equation 2 around the y axis is used and the tip radius was estimated using an iterative approach where image

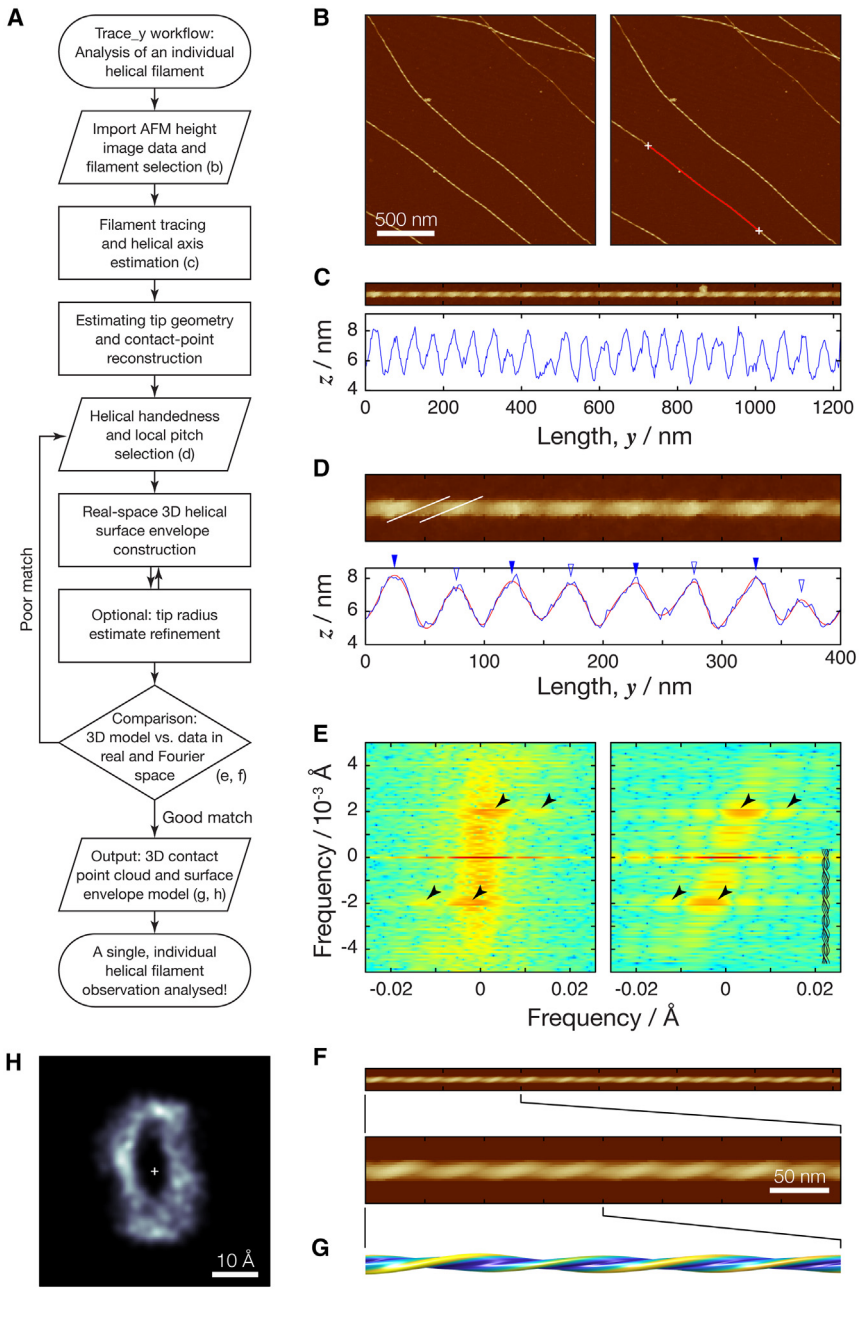

Figure 1. The Trace_y workflow demonstrated on an individual Aβ_{42} amyloid fibril

(A) Flowchart overview of the Trace_y workflow for analyzing the structure of an individual helical filament.

(B) Topographical AFM height images of helical twisted Aβ_{42} fibrils. The right image is identical to the left image, except with an example fibril and its central contour line highlighted (red line). The white crosses indicate user defined start and endpoint of the traced fibril segment. The scale bar represent 500 nm in both images.

(C) Digitally straightened fibril image showing the fibril highlighted in (B) and its central line height profile.

(D) A zoomed image showing the first 400 nm segment the same fibril shown in (C). Its central line height profile (blue line) is shown together with a digitally smoothed line (red line), where the peak positions were determined (blue triangles). The filled blue triangles indicate reference locations with one helical pitch distance in between each filled blue triangles.

(E) Power spectrum of 2D Fourier transform of the fibril image data is shown to the left compared with a spectrum calculated from a simulated topograph image shown to the right. The black arrows indicate identical locations in both power spectra and show major peak locations.

(F and G) Topographic AFM height image (F) simulated from the 3D fibril envelope model (G) of the same fibril in (B) together with a zoomed in image showing the first 400 nm segment.

(H) The cross-sectional contact-point density map of the same highlighted fibril from (B). The density map is constructed using the whole of the filament segment shown in (B) and the scale bar indicates distance of 10 Å.

dilation caused by the contact between the tip model and the circular cross-section of a featureless cylinder is matched to the experimentally observed dilation for the analyzed filament. This procedure is illustrated by Figure 3A, where least-squares regression analysis is performed with a calculated convoluted cross-section (red lines and crosses) of a featureless cylinder (black) fit to the observed convoluted cross-section of the filament averaged through the length of the filament along its estimated helical axis (blue circles). This approach is able to provide a useful initial tip radius estimate using the helical axis coordinates as input since the cross-section of a helical structure with its cross-section rotating around its helical axis approaches a circular shape when averaged over the length of its helical axis.

The initial tip radius estimate, and subsequently also an estimate of the magnitude of the dilation for each pixel coordinate, can be further optimized in a later optional step by minimizing the difference between the image data of the filament and a simulated image back-calculated using the surface envelope model of the same filament. An important advantage of this sample feature-based blind tip radius estimation approach is that additional dedicated tip characterization step, which can additionally blunt the tip during characterization, can be avoided.

Once the tip radius is estimated, deconvolution of the image data by CPR using the same principles of rigid-body interactions between the AFM probe tip and the sample filament used in the previous step[14] was subsequently carried out to recover the 3D coordinates of tip-sample contact points (Figures 3B–3D). This step outputs a point cloud containing the estimated tip-sample surface contact points by moving the 3D x/y/z coordinates of the recorded tip positions off the x/y pixel lattice of the image to the appropriate sub-pixel locations estimated by CPR step. Figure 3B shows the AFM height image of a segment of the

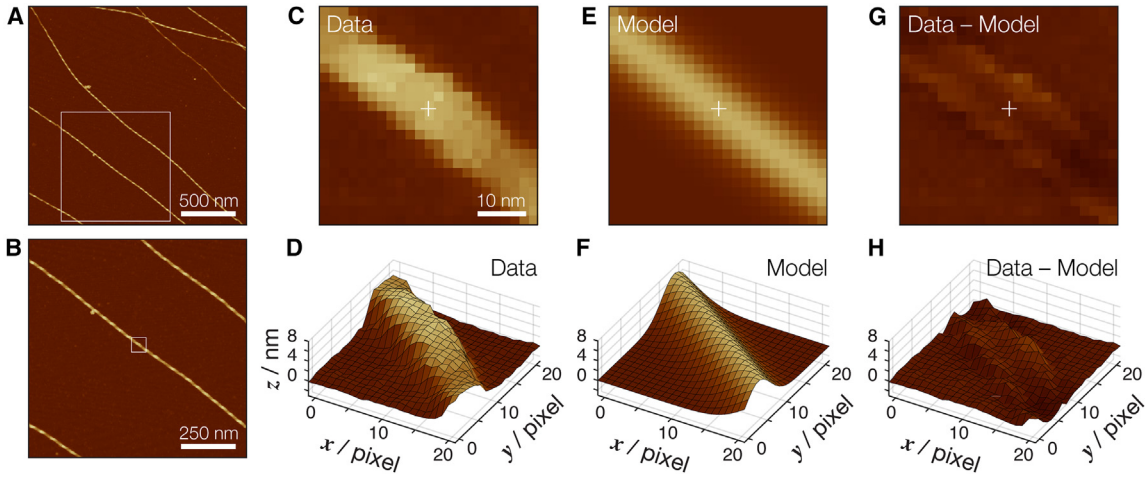

Figure 2. Tracing of individual filaments and estimation of helical axis coordinates by regression analysis using a curved Gaussian wall model

(A) Example topographical AFM height images of helical twisted Aβ_{42} fibrils. The same 2 × 2 μm image as Figure 1B is shown. The white box indicates 1 × 1 μm magnified area shown in (b) and scale bar indicating 500 nm.

(B) 1 × 1 μm magnified area indicated by the white box in (A), with the scale bar indicating 250 nm.

(C and D) 22 × 22 pixel area indicated in the image data in (B) shown as a 2D height image and as a 3D surface, respectively.

(E and F) Best fit curved Gaussian wall model of the same area indicated in the image data in (B) shown as a 2D height image and as a 3D surface, respectively.

(G and H) Pixel level residuals between the image data and the best fit model shown as a 2D height image and as a 3D surface, respectively.

In (C–H), white cross indicates an estimated point of the helical axis x/y coordinates. Scale bar indicate 10 nm in (C, E, and G).

example Aβ_{42} filament where each pixel is shown as a point in 3D space. All of the points have their x/y coordinates in the pixel lattice of the image, and the pixel lattice along the x axis is particularly visible from the viewing angle used in Figure 3B. Figure 3C demonstrates the tip-sample contact point cloud after image deconvolution by CPR where the data points are no longer bound to the x/y pixel lattice and instead echo the actual sample surface coordinates. The points that are localized at the top of the filament (red points in Figure 3D) were then selected to be used in subsequent steps to create a surface envelope model of the individual filament. In summary, the CPR step reconstructed the 3D contact points between the AFM tip and the filament, creating a point cloud that represents the top of the individual filament being analyzed.

Visualization of the filament cross-section and construction of 3D surface envelope model

The point cloud data that represents the structure of the filament top obtained from the CPR step was next used to create a 3D surface envelope model of the filament for visualization. The helical properties of the individual filament being analyzed were first determined by manual inspection. This is shown for the example Aβ_{42} filament in Figures 1C–1E. Since topological AFM height images are not transmission images, only one

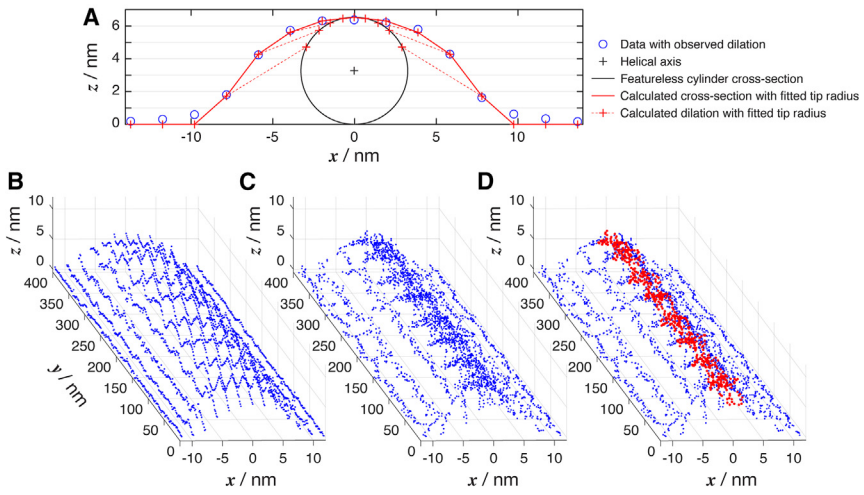

Figure 3. Cantilever tip radius estimation and contact point reconstruction result in a 3D point cloud that represents the tip-filament surface contact points

(A) Initial estimation of the tip radius by least-squares fit of calculated image dilation (red crosses, red solid line and red dotted lines) from a featureless cylinder (black line representing the cross-section of the cylinder) to observed average dilation along the fibril (blue circles).

(B) The fibril image in Figure 1D shown as points in 3D space representing the pixels' x/y/z coordinates.

(C) The point cloud output of CPR showing the x/y/z coordinates of the points in (B) moved to estimated tip-filament surface contact points.

(D) Contact points on the top of the helical filament subsequently used for construction of 3D surface envelop is show as red points.

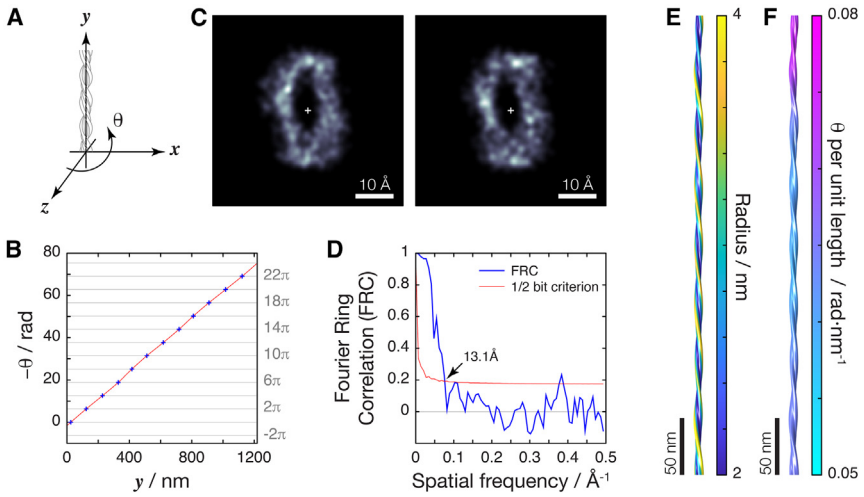

Figure 4. Construction of filament 3D surface envelope by point cloud registration in a helical coordinate system

(A) Schematic of the helical coordinate system used to align contact points in a point cloud representing a helical filament. The x/z plane of this coordinate system is set to rotate around the helical axis aligned to the y axis with the same twist angles θ as observed for the filament.

(B) The local twist angle θ (blue cross) of the example filament shown in Figure 1C measured using its height profile (e.g., filled blue triangles in Figure 1D). Red line represents the θ function along the whole filament constructed by spline interpolation with the measurement points (blue cross).

(C) The cross-sectional contact-point density map of the same example filament. An example density map pair generated by randomly selected half-sets of the contact point cloud used for FRC measurement is shown.

(D) The spatial resolution of the contact-point density map shown in Figure 1H estimated by FRC (blue line) and the ½ bit information criterion[40] (red line with the FRC crossing point indicated by the arrow).

(E) 3D surface envelope model of the example filament (the first 400 nm segment as shown in Figure 1D) with surface color indicating distance to helical axis.

(F) The same 3D surface envelope model of the example filament as (E) but with color indicating helical twist mapped to its surface to highlight local helical structural features.

side of the helical filament is observed. Hence, the helical handedness of the filament twist is typically readily visible by the tilt direction of the striation pattern (exemplified by the white lines in Figure 1D). For left-hand twisted filaments, the tilt of the pattern goes from bottom left to top right whereas the tilt of the pattern goes from bottom right to top left for right-hand twisted fibrils when the filaments image is aligned horizontally. The handedness can also be deduced by 2D Fourier transform of the filament image (Figure 1E). For vertically aligned filaments images, the main peaks in the 2D Fourier transform power spectrum image follow the same bottom left to top right or bottom right to top left tilt patterns relative to the image center for left-handed or right-handed twists, respectively (arrow heads in Figure 1E for the example Aβ_{42} filament). The helical pitch of the filament can be deduced from the z-height peak patterns of the central contour line of the filament image, and the peaks in the 2D Fourier transform of the filament image. In this case, a direct determination of the helical pitch by spotting repeating patterns in the z-height profile or estimating the magnitude of the tilt of the pattern in 2D Fourier transformed image may not be straightforward as the differences expected for different cross-sectional symmetries may be small. Therefore, a best guess of the cross-sectional symmetry and resulting helical pitch was used for the initial 3D model building, and the validity of this initial guess was checked by comparing simulated image and its 2D Fourier transform power spectrum with the image data of the filament in a subsequent step. This is illustrated for the example Aβ_{42} filament in Figure 1D where the helical pitch was estimated to be the peak-peak distances of every-other peak in the central line z-height profile of the filament (e.g., filled blue triangles in Figure 1D), possibly due to a C_2 cross-sectional symmetry or a 2_1-screw axis symmetry. This guess for the example filament was validated because the simulated image based on the 3D model constructed using the guessed pitch values (Figure 1F) matched well with the image data, and the location of the main peaks in the 2D Fourier transformed image matched with those in the 2D Fourier transformed power spectrum image of the data (arrow heads in Figure 1E).

Once the helical pitch and twist handedness is determined for the individual filament being analyzed, the point cloud data representing the structure of the filament top is moved from its original AFM height image coordinate system to a helical coordinate system (Figure 4A) where the helical axis of the filament is aligned with the y axis and the x/z-axes (the cross-sectional plane) rotates with the same rate along the helical axis as the helical filament being analyzed. In this case, the x/z plane rotates with a θ rotation angle that is locally estimated, referenced onto the same peaks used to calculate the local helical pitch values (filled blue triangles in Figure 1D). For the example Aβ_{42} filament, the θ rotation angle at any given y coordinate along the helical axis is shown in Figure 4B where the blue crosses are the local reference points at full integral number of complete turns around the helical axis, and the red line represents the interpolated θ values along the helical axis by cubic splines interpolation. The cross-sectional envelope of the helical filament was then visualized on the helical x/z plane when the point cloud was registered onto the rotating x/z-frame. Figure 1H shows the visualization of the cross-sectional envelope of the example Aβ_{42} filament segment as a density map of the contact points in the x/z-plane constructed using a non-parametric Gaussian kernel density estimator[41] (Equation 3). The spatial resolution of this density map was subsequently estimated by a Monte Carlo (MC) approach where the points in the point cloud were randomly split into two equal sized sets. The density map of each set of points were separately constructed (an example pair is shown in Figure 4C) and their Fourier ring correlation were evaluated using the ½-bit information criterion[40] (Equations 4 and 5, respectively). For the example Aβ_{42} filament segment shown in Figure 1H, evaluated using 500 MC cycles, the resulting spatial resolution estimate was around 13.1 Å (Figure 4D).

Finally, the 3D surface envelope of the whole of the filament was also visualized. This was achieved by least-squares spline fitting an average cross-sectional envelope represented by a

Table 1. Summary of existing open-source AFM data analysis software relevant and useful for individual filament level structural analyses, and comparison with Trace_y

Software tool	Web URL	Capability	Status and reference
Gwyddion	http://gwyddion.net	General image visualization and processing software for AFM topological height images as well as data from a range of other AFM imaging modes.	Gwyddion is originally described in Necas & Klapetek (2012)[45] and was updated to version 2.66 as of May 2024.
FiberApp	https://github.com/ivan-usov/FiberApp	Analysis software tool for AFM topological height images with emphasis on filament tracing and statistical analysis of the filaments.	FiberApp is described in Usov & Mezzenga (2015)[46] and was last updated in 2018.
TopoStats	https://github.com/AFM-SPM/TopoStats	Processing and analysis software tool for AFM topological height images with emphasis on linear or circular DNA contour tracing and extraction of statistical information.	TopoStats is described in Beton et al. (2021)[44] and was updated to v2.2.1 as of June 2024.
NanoLocz	https://github.com/George-R-Heath/NanoLocz	Processing and analysis software tool for High-Speed AFM topological height images and videos with emphasis on particle tracking and localization-AFM (L-AFM) analysis.	NanoLocz is described in Heath et al. (2024)[47] and was updated to v1.20 as of May 2024
Trace_y	https://github.com/wfxue/Trace_y	AFM image analysis software tool with emphasis on individual helical filament structures described in this report. Generates 3D contact point clouds from AFM height images and performs tracing and 3D structural reconstruction of helical filaments.	Described in this report, and current version 7 as of November 2024

cubic spline curve in the x/z-plane at gridded y coordinates of the point cloud data along the helical axis. A moving window approach to select only points in the point-cloud local to each evaluated y coordinate (within ±1 helical pitch distance in their y coordinate along the helical axis) were used to construct cross-sectional envelopes that takes into account local structural variations as previously described.[14] The final 3D surface envelope of a 400 nm segment of the example $A\beta_{42}$ filament is shown in Figures 4E and 4F. For multimodal visualization of structural, nano-mechanical, or physicochemical properties, the filament 3D model surface coordinates can be correlated and color-coded according to data from other AFM channels, for example stiffness, deformation, or infrared absorption. Here, the example filament model was colored by its local structural features, specifically by the perpendicular distance to the helical axis in Figure 4E to highlight its helical properties and by its local twist angle per unit length in Figure 4F to highlight the structural variations in its twist along this single individual filament.

DISCUSSION

Atomic force microscopy has recently embarked on a renaissance in terms of its application in imaging of biological/soft materials and in molecular and structural biology, driven by the recent developments in high-speed AFM instrumentation[42] and several new emerging image analysis algorithms and tools[9,14,43–47] (Table 1). AFM imaging has already led to new structural insights for example with bacterial cell walls,[11] ion channels,[48] DNA,[49] and intrinsically disordered proteins.[50] Despite the limitations of the AFM physics due to the nanometer size of the probe tip and that only the surface features of molecules of interest are probed, AFM is capable of time-resolved imaging with ~100 ms temporal resolution in aqueous conditions, allowing the dynamics of molecules to be studied under ambient conditions. AFM is also capable of high signal-to-noise topology imaging with typically sub Ångström noise and ~1 Å resolution in the z height-axis. This feature allows for structural analysis of individual molecules without cross-molecule averaging.[13,14,35] This allows the structural variations between individual molecules in a population or within the same molecular assembly to be resolved and quantified.[13,35] For example, the structural population distribution of polymorphous $A\beta_{42}$ amyloid fibrils has been recently resolved, and the heterogeneity of the population under different conditions as well as the dissimilarities between individual filament structures in the population distribution was quantified. Individual filament level analysis also resulted in the ability to analyze and identify rare fibril species within the heterogeneous $A\beta_{42}$ amyloid populations.[35] Thus, the two notable features of AFM, the abilities to study individual molecules and their dynamics, fill an important gap in the type of molecular structural information that can be gained, and create an unique niche for AFM in structural biology where methods, such as cryo-electron microscopy, nuclear magnetic resonance spectroscopy, and X-ray crystallography all provide ensemble averaged structural information.

Here, the high signal-to-noise topology imaging feature of AFM is exploited to allow 3D structural studies of individual helical filaments such as amyloid protein fibrils. Recent structural analysis of individual amyloid fibrils formed from a tau sequence[37,51] and from a β2-microglobulin variant[52] by AFM carried out in parallel with cryo-electron microscopy has validated that the 3D surface

envelopes of the individual filaments analyzed by Trace_y indeed match with the cryo-electron microscopy derived maps of identical filament species. These cases demonstrated the accuracy of the Trace_y 3D-reconstruction algorithm and provided validating evidence for structural analysis helical amyloid fibrils using Trace_y. The Trace_y 3D-reconstruction algorithm requires helical filaments of at least one to two helical pitch in length, and only partial reconstruction of the top surfaces can be achieved at individual filament level by CPR-AFM for very short filaments or filaments without sufficient helical twist where one helical pitch or more in length is not observed. Currently, the Trace_y workflow assumes no substantial deformations of the filaments at low imaging forces used in the experiments. Inclusion of possible deformations models, particularly in the helical axis of the filament used to axis-align the 3D point clouds of the filaments, could further improve the accuracy of the 3D reconstruction.

The Trace_y software and the workflow based on 3D CPR-AFM presented here is a post-experiment analysis approach. As such, it is widely applicable for the analysis of topographical AFM height images. Importantly, the application of Trace_y on helical amyloid fibrils demonstrated here show unequivocally that 3D structural reconstruction is possible using AFM image data as input. The CPR approach allows this by unlocking the 3D information encoded in the topological images and show that this information can be understood and visualized as 3D contact point clouds. Contact point clouds can be quantitatively analyzed once aligned to an appropriate and meaningful coordinate system and/or to each other, this is a process also referred to as point cloud registration. Indeed, point cloud registration is a principal problem that features prominently in pattern recognition and computer vision fields. In the case of Trace_y, the current presented version of the 3D reconstruction workflow and the algorithms that underpin the key steps of the workflow establishes many opportunities for further developments, refinements and improvements at each and every step by the bio-AFM community. For example, refinements to the helical axis estimate and subsequently the alignment of the cross-sectional axes will improve the overall quality of the 3D point cloud in representing the surface envelope of the helical structures of interest. Integrative approaches involving spatial 3D data sources from cryo-EM, molecular PDB models from NMR or X-ray crystallography studies, or predicted molecular models or designs (e.g., by AlphaFold[53] and Rosetta[54]) can further extend the use of the 3D point cloud data and provide models by which the point clouds can be compared to or registered onto. In addition, it may be possible to map chemical or nanomechanical information onto the 3D surface envelopes (e.g., using analogous approach as demonstrated in Figures 4E and 4F) reconstructed from multi-modal AFM-IR, AFM-Raman, or AFM nano-mechanics experiments. Therefore, these opportunities may make it possible to distinguish between different conformational or ligand binding states of biological molecules or complexes, facilitating the analysis of protein structure and function to high details on a single, individual molecule level.

RESOURCE AVAILABILITY

Lead contact

Requests for further information and resources should be directed to and will be fulfilled by the lead contact, Wei-Feng Xue (w.f.xue@kent.ac.uk).

Materials availability

This study did not generate new unique reagents.

Data and code availability

- All data reported in this paper will be shared by the lead contact upon request.
- The original code reported in this paper is publicly available as of the date of publication as an open-source software at https://github.com/wfxue/Trace_y.
- Any additional information required to re-analyze the data reported in this paper is available from the lead contact upon request.

ACKNOWLEDGMENTS

Help with the software development and insightful discussions by Liisa Lutter, and acquisition of the $A\beta_{42}$ amyloid image data used here as examples by Liam Aubrey are gratefully acknowledged. Testing and helpful comments provided by the members of the Xue and the Louise Serpell research groups are also gratefully acknowledged. The AFM image examples used is acquired on an instrument supported by funding from the Biotechnology and Biological Sciences Research Council (BBSRC), UK grants BB/J008001/1, BB/M02427X/1, and BB/S003312/1, and UK Engineering and Physical Sciences Research Council (EPSRC) New Horizons grant EP/X01729X/1.

AUTHOR CONTRIBUTIONS

W.-F.X. is the sole author of this paper.

DECLARATION OF INTERESTS

The author declares no competing interests.

STAR★METHODS

Detailed methods are provided in the online version of this paper and include the following:

- KEY RESOURCES TABLE
- METHOD DETAILS
  - AFM specimen preparation
  - Topographical AFM image data acquisition
  - Initial image processing
- QUANTIFICATION AND STATISTICAL ANALYSIS

Received: June 3, 2024
Revised: October 22, 2024
Accepted: November 11, 2024
Published: December 5, 2024

REFERENCES

1. Dufrêne, Y.F., Ando, T., Garcia, R., Alsteens, D., Martinez-Martin, D., Engel, A., Gerber, C., and Muller, D.J. (2017). Imaging modes of atomic force microscopy for application in molecular and cell biology. Nat. Nanotechnol. *12*, 295–307. https://doi.org/10.1038/nnano.2017.45.
2. Parsons, E.S., Stanley, G.J., Pyne, A.L.B., Hodel, A.W., Nievergelt, A.P., Menny, A., Yon, A.R., Rowley, A., Richter, R.P., Fantner, G.E., et al. (2019). Single-molecule kinetics of pore assembly by the membrane attack complex. Nat. Commun. *10*, 2066. https://doi.org/10.1038/s41467-019-10058-7.
3. Chen, Y., Radford, S.E., and Brockwell, D.J. (2015). Force-induced remodelling of proteins and their complexes. Curr. Opin. Struct. Biol. *30*, 89–99. https://doi.org/10.1016/j.sbi.2015.02.001.
4. Ares, P., Fuentes-Perez, M.E., Herrero-Galán, E., Valpuesta, J.M., Gil, A., Gomez-Herrero, J., and Moreno-Herrero, F. (2016). High resolution atomic force microscopy of double-stranded RNA. Nanoscale *8*, 11818–11826. https://doi.org/10.1039/c5nr07445b.

5. Moreno-Herrero, F., Pérez, M., Baró, A.M., and Avila, J. (2004). Characterization by atomic force microscopy of Alzheimer paired helical filaments under physiological conditions. Biophys. J. *86*, 517–525. https://doi.org/10.1016/S0006-3495(04)74130-2.

6. Nowakowski, R., Luckham, P., and Winlove, P. (2001). Imaging erythrocytes under physiological conditions by atomic force microscopy. Biochim. Biophys. Acta *1514*, 170–176. https://doi.org/10.1016/s0005-2736(01)00365-0.

7. Cappella, B., and Dietler, G. (1999). Force-distance curves by atomic force microscopy. Surf. Sci. Rep. *34*, 1–104. https://doi.org/10.1016/S0167-5729(99)00003-5.

8. Gross, L., Mohn, F., Moll, N., Liljeroth, P., and Meyer, G. (2009). The chemical structure of a molecule resolved by atomic force microscopy. Science *325*, 1110–1114. https://doi.org/10.1126/science.1176210.

9. Heath, G.R., Kots, E., Robertson, J.L., Lansky, S., Khelashvili, G., Weinstein, H., and Scheuring, S. (2021). Localization atomic force microscopy. Nature *594*, 385–390. https://doi.org/10.1038/s41586-021-03551-x.

10. Drake, B., Prater, C.B., Weisenhorn, A.L., Gould, S.A., Albrecht, T.R., Quate, C.F., Cannell, D.S., Hansma, H.G., and Hansma, P.K. (1989). Imaging crystals, polymers, and processes in water with the atomic force microscope. Science *243*, 1586–1589. https://doi.org/10.1126/science.2928794.

11. Pasquina-Lemonche, L., Burns, J., Turner, R.D., Kumar, S., Tank, R., Mullin, N., Wilson, J.S., Chakrabarti, B., Bullough, P.A., Foster, S.J., and Hobbs, J.K. (2020). The architecture of the Gram-positive bacterial cell wall. Nature *582*, 294–297. https://doi.org/10.1038/s41586-020-2236-6.

12. Radmacher, M., Tillamnn, R.W., Fritz, M., and Gaub, H.E. (1992). From molecules to cells: imaging soft samples with the atomic force microscope. Science *257*, 1900–1905. https://doi.org/10.1126/science.1411505.

13. Aubrey, L.D., Blakeman, B.J.F., Lutter, L., Serpell, C.J., Tuite, M.F., Serpell, L.C., and Xue, W.F. (2020). Quantification of amyloid fibril polymorphism by nano-morphometry reveals the individuality of filament assembly. Commun. Chem. *3*, 125. https://doi.org/10.1038/s42004-020-00372-3.

14. Lutter, L., Serpell, C.J., Tuite, M.F., Serpell, L.C., and Xue, W.F. (2020). Three-dimensional reconstruction of individual helical nano-filament structures from atomic force microscopy topographs. Biomol. Concepts *11*, 102–115. https://doi.org/10.1515/bmc-2020-0009.

15. Lutter, L., Aubrey, L.D., and Xue, W.F. (2021). On the Structural Diversity and Individuality of Polymorphic Amyloid Protein Assemblies. J. Mol. Biol. *433*, 167124. https://doi.org/10.1016/j.jmb.2021.167124.

16. Knowles, T.P.J., Vendruscolo, M., and Dobson, C.M. (2014). The amyloid state and its association with protein misfolding diseases. Nat. Rev. Mol. Cell Biol. *15*, 384–396. https://doi.org/10.1038/nrm3810.

17. Eisenberg, D., and Jucker, M. (2012). The amyloid state of proteins in human diseases. Cell *148*, 1188–1203. https://doi.org/10.1016/j.cell.2012.02.022.

18. Ke, P.C., Zhou, R., Serpell, L.C., Riek, R., Knowles, T.P.J., Lashuel, H.A., Gazit, E., Hamley, I.W., Davis, T.P., Fändrich, M., et al. (2020). Half a century of amyloids: past, present and future. Chem. Soc. Rev. *49*, 5473–5509. https://doi.org/10.1039/c9cs00199a.

19. Scheres, S.H., Zhang, W., Falcon, B., and Goedert, M. (2020). Cryo-EM structures of tau filaments. Curr. Opin. Struct. Biol. *64*, 17–25. https://doi.org/10.1016/j.sbi.2020.05.011.

20. Lutter, L., Serpell, C.J., Tuite, M.F., and Xue, W.F. (2019). The molecular lifecycle of amyloid - Mechanism of assembly, mesoscopic organisation, polymorphism, suprastructures, and biological consequences. Biochim. Biophys. Acta, Proteins Proteomics *1867*, 140257. https://doi.org/10.1016/j.bbapap.2019.07.010.

21. Hervas, R., Rau, M.J., Park, Y., Zhang, W., Murzin, A.G., Fitzpatrick, J.A.J., Scheres, S.H.W., and Si, K. (2020). Cryo-EM structure of a neuronal functional amyloid implicated in memory persistence in Drosophila. Science *367*, 1230–1234. https://doi.org/10.1126/science.aba3526.

22. Léger, P., Nachman, E., Richter, K., Tamietti, C., Koch, J., Burk, R., Kummer, S., Xin, Q., Stanifer, M., Bouloy, M., et al. (2020). NSs amyloid formation is associated with the virulence of Rift Valley fever virus in mice. Nat. Commun. *11*, 3281. https://doi.org/10.1038/s41467-020-17101-y.

23. Adamcik, J., and Mezzenga, R. (2018). Amyloid Polymorphism in the Protein Folding and Aggregation Energy Landscape. Angew. Chem., Int. Ed. Engl. *57*, 8370–8382. https://doi.org/10.1002/anie.201713416.

24. Ruggeri, F.S., Flagmeier, P., Kumita, J.R., Meisl, G., Chirgadze, D.Y., Bongiovanni, M.N., Knowles, T.P.J., and Dobson, C.M. (2020). The Influence of Pathogenic Mutations in alpha-Synuclein on Biophysical and Structural Characteristics of Amyloid Fibrils. ACS Nano *14*, 5213–5222. https://doi.org/10.1021/acsnano.9b09676.

25. Koloteva-Levine, N., Aubrey, L.D., Marchante, R., Purton, T.J., Hiscock, J.R., Tuite, M.F., and Xue, W.F. (2021). Amyloid particles facilitate surface-catalyzed cross-seeding by acting as promiscuous nanoparticles. Proc. Natl. Acad. Sci. USA *118*, e2104148118. https://doi.org/10.1073/pnas.2104148118.

26. Buell, A.K., Galvagnion, C., Gaspar, R., Sparr, E., Vendruscolo, M., Knowles, T.P.J., Linse, S., and Dobson, C.M. (2014). Solution conditions determine the relative importance of nucleation and growth processes in alpha-synuclein aggregation. Proc. Natl. Acad. Sci. USA *111*, 7671–7676. https://doi.org/10.1073/pnas.1315346111.

27. Marchante, R., Beal, D.M., Koloteva-Levine, N., Purton, T.J., Tuite, M.F., and Xue, W.F. (2017). The physical dimensions of amyloid aggregates control their infective potential as prion particles. Elife *6*, e27109. https://doi.org/10.7554/eLife.27109.

28. Sanami, S., Purton, T.J., Smith, D.P., Tuite, M.F., and Xue, W.F. (2022). Comparative Analysis of the Relative Fragmentation Stabilities of Polymorphic Alpha-Synuclein Amyloid Fibrils. Biomolecules *12*, 630. https://doi.org/10.3390/biom12050630.

29. Beal, D.M., Tournus, M., Marchante, R., Purton, T.J., Smith, D.P., Tuite, M.F., Doumic, M., and Xue, W.F. (2020). The Division of Amyloid Fibrils: Systematic Comparison of Fibril Fragmentation Stability by Linking Theory with Experiments. iScience *23*, 101512. https://doi.org/10.1016/j.isci.2020.101512.

30. Xue, W.F., and Radford, S.E. (2013). An imaging and systems modeling approach to fibril breakage enables prediction of amyloid behavior. Biophys. J. *105*, 2811–2819. https://doi.org/10.1016/j.bpj.2013.10.034.

31. Xue, W.F., Hellewell, A.L., Gosal, W.S., Homans, S.W., Hewitt, E.W., and Radford, S.E. (2009). Fibril fragmentation enhances amyloid cytotoxicity. J. Biol. Chem. *284*, 34272–34282. https://doi.org/10.1074/jbc.M109.049809.

32. Chitty, C., Kuliga, K., and Xue, W.F. (2024). Atomic force microscopy 3D structural reconstruction of individual particles in the study of amyloid protein assemblies. Biochem. Soc. Trans. *52*, 761–771. https://doi.org/10.1042/BST20230857.

33. Goldsbury, C., Frey, P., Olivieri, V., Aebi, U., and Müller, S.A. (2005). Multiple assembly pathways underlie amyloid-beta fibril polymorphisms. J. Mol. Biol. *352*, 282–298. https://doi.org/10.1016/j.jmb.2005.07.029.

34. Feuillie, C., Lambert, E., Ewald, M., Azouz, M., Henry, S., Marsaudon, S., Cullin, C., Lecomte, S., and Molinari, M. (2020). Cryo-EM structure of a neuronal functional amyloid implicated in memory persistence in Drosophila. Front. Mol. Biosci. *7*, 571696. https://doi.org/10.3389/fmolb.2020.571696.

35. Aubrey, L.D., Lutter, L., Fennell, K., Purton, T.J., Ward, N., Serpell, L.C., and Xue, W.-F. (2023). Structural reconstruction of individual filaments in Abeta42 fibril populations assembled *in vitro* reveal rare species that resemble ex vivo amyloid polymorphs from human brains. Preprint at bioRxiv. https://doi.org/10.1101/2023.07.14.549001.

36. Konstantoulea, K., Guerreiro, P., Ramakers, M., Louros, N., Aubrey, L.D., Houben, B., Michiels, E., De Vleeschouwer, M., Lampi, Y., Ribeiro, L.F., et al. (2022). Heterotypic Amyloid beta interactions facilitate amyloid assembly and modify amyloid structure. EMBO J. *41*, e108591. https://doi.org/10.15252/embj.2021108591.

37. Lutter, L., Al-Hilaly, Y.K., Serpell, C.J., Tuite, M.F., Wischik, C.M., Serpell, L.C., and Xue, W.F. (2022). Structural Identification of Individual Helical Amyloid Filaments by Integration of Cryo-Electron Microscopy-Derived Maps in Comparative Morphometric Atomic Force Microscopy Image Analysis. J. Mol. Biol. *434*, 167466. https://doi.org/10.1016/j.jmb.2022.167466.

38. Villarrubia, J.S. (1997). Algorithms for Scanned Probe Microscope Image Simulation, Surface Reconstruction, and Tip Estimation. J. Res. Natl. Inst. Stand. Technol. *102*, 425–454. https://doi.org/10.6028/jres.102.030.

39. Ruhnow, F., Zwicker, D., and Diez, S. (2011). Tracking single particles and elongated filaments with nanometer precision. Biophys. J. *100*, 2820–2828. https://doi.org/10.1016/j.bpj.2011.04.023.

40. van Heel, M., and Schatz, M. (2005). Fourier shell correlation threshold criteria. J. Struct. Biol. *151*, 250–262. https://doi.org/10.1016/j.jsb.2005.05.009.

41. Botev, Z.I., Grotowski, J.F., and Kroese, D.P. (2010). Kernel Density Estimation Via Diffusion. Ann Stat. *38*, 2916–2957. https://doi.org/10.1214/10-Aos799.

42. Flechsig, H., and Ando, T. (2023). Protein dynamics by the combination of high-speed AFM and computational modeling. Curr. Opin. Struct. Biol. *80*, 102591. https://doi.org/10.1016/j.sbi.2023.102591.

43. Amyot, R., and Flechsig, H. (2020). BioAFMviewer: An interactive interface for simulated AFM scanning of biomolecular structures and dynamics. PLoS Comput. Biol. *16*, e1008444. https://doi.org/10.1371/journal.pcbi.1008444.

44. Beton, J.G., Moorehead, R., Helfmann, L., Gray, R., Hoogenboom, B.W., Joseph, A.P., Topf, M., and Pyne, A.L.B. (2021). TopoStats - A program for automated tracing of biomolecules from AFM images. Methods *193*, 68–79. https://doi.org/10.1016/j.ymeth.2021.01.008.

45. Necas, D., and Klapetek, P. (2012). Gwyddion: an open-source software for SPM data analysis. Cent. Eur. J. Phys. *10*, 181–188. https://doi.org/10.2478/s11534-011-0096-2.

46. Usov, I., and Mezzenga, R. (2015). FiberApp: An Open-Source Software for Tracking and Analyzing Polymers, Filaments, Biomacromolecules, and Fibrous Objects. Macromolecules *48*, 1269–1280. https://doi.org/10.1021/ma502264c.

47. Heath, G.R., Micklethwaite, E., and Storer, T.M. (2024). NanoLocz: Image Analysis Platform for AFM, High-Speed AFM, and Localization AFM. Small Methods *8*, e2301766. https://doi.org/10.1002/smtd.202301766.

48. Lansky, S., Betancourt, J.M., Zhang, J., Jiang, Y., Kim, E.D., Paknejad, N., Nimigean, C.M., Yuan, P., and Scheuring, S. (2023). A pentameric TRPV3 channel with a dilated pore. Nature *621*, 206–214. https://doi.org/10.1038/s41586-023-06470-1.

49. Pyne, A.L.B., Noy, A., Main, K.H.S., Velasco-Berrelleza, V., Piperakis, M.M., Mitchenall, L.A., Cugliandolo, F.M., Beton, J.G., Stevenson, C.E.M., Hoogenboom, B.W., et al. (2021). Base-pair resolution analysis of the effect of supercoiling on DNA flexibility and major groove recognition by triplex-forming oligonucleotides. Nat. Commun. *12*, 1053. https://doi.org/10.1038/s41467-021-21243-y.

50. Kodera, N., Noshiro, D., Dora, S.K., Mori, T., Habchi, J., Blocquel, D., Gruet, A., Dosnon, M., Salladini, E., Bignon, C., et al. (2021). Structural and dynamics analysis of intrinsically disordered proteins by high-speed atomic force microscopy. Nat. Nanotechnol. *16*, 181–189. https://doi.org/10.1038/s41565-020-00798-9.

51. Lövestam, S., Koh, F.A., van Knippenberg, B., Kotecha, A., Murzin, A.G., Goedert, M., and Scheres, S.H.W. (2022). Assembly of recombinant tau into filaments identical to those of Alzheimer's disease and chronic traumatic encephalopathy. Elife *11*, e76494. https://doi.org/10.7554/eLife.76494.

52. Wilkinson, M., Gallardo, R.U., Martinez, R.M., Guthertz, N., So, M., Aubrey, L.D., Radford, S.E., and Ranson, N.A. (2023). Disease-relevant β2-microglobulin variants share a common amyloid fold. Nat. Commun. *14*, 1190. https://doi.org/10.1038/s41467-023-36791-8.

53. Jumper, J., Evans, R., Pritzel, A., Green, T., Figurnov, M., Ronneberger, O., Tunyasuvunakool, K., Bates, R., Žídek, A., Potapenko, A., et al. (2021). Highly accurate protein structure prediction with AlphaFold. Nature *596*, 583–589. https://doi.org/10.1038/s41586-021-03819-2.

54. Leman, J.K., Weitzner, B.D., Lewis, S.M., Adolf-Bryfogle, J., Alam, N., Alford, R.F., Aprahamian, M., Baker, D., Barlow, K.A., Barth, P., et al. (2020). Macromolecular modeling and design in Rosetta: recent methods and frameworks. Nat. Methods *17*, 665–680. https://doi.org/10.1038/s41592-020-0848-2.

55. Yang, Y., Arseni, D., Zhang, W., Huang, M., Lövestam, S., Schweighauser, M., Kotecha, A., Murzin, A.G., Peak-Chew, S.Y., Macdonald, J., et al. (2022). Cryo-EM structures of amyloid-beta 42 filaments from human brains. Science *375*, 167–172. https://doi.org/10.1126/science.abm7285.

56. O'Malley, T.T., Linse, S., and Walsh, D.M. (2018). Production and Use of Recombinant Abeta for Aggregation Studies. Methods Mol. Biol. *1777*, 307–320. https://doi.org/10.1007/978-1-4939-7811-3_19.

STAR★METHODS

KEY RESOURCES TABLE

REAGENT or RESOURCE	SOURCE	IDENTIFIER
Software and algorithms		
Trace_y (version 7)	This paper	https://github.com/wfxue/Trace_y
MATLAB (release 2024a)	MathWorks	https://www.mathworks.com/products/matlab.html
Other		
Bruker MultiMode 8 scanning probe microscope with Nanoscope V controller	Bruker	https://www.bruker.com/en/products-and-solutions/microscopes/materials-afm.html

METHOD DETAILS

AFM specimen preparation

The 3D contact-point reconstruction AFM (CPR-AFM) workflow to analyse the 3D surface envelopes of individual helical filaments using Trace_y is demonstrated on amyloid fibrils formed from the 42 residues long Amyloid β 1-42 peptide ($A\beta_{42}$). Helical filaments formed from $A\beta_{42}$ is associated with neurodegenerative diseases such as Alzheimer's disease (AD), in which extracellular deposits known as plaques containing $A\beta_{42}$ amyloid fibrils are found in brains of patients.[55] Here, fibrils were formed *in vitro* from recombinant $A\beta_{42}$[56] in 20mM HEPES buffer under quiescent conditions at pH 7.4 and 37°C.[35] The fibrils were deposited onto freshly cleaved mica discs as previously described.[35]

Topographical AFM image data acquisition

$A\beta_{42}$ amyloid fibrils were imaged by AFM using a Multimode 8 SPM with a Nanoscope V controller (Bruker) operating under peak-force tapping mode as detailed previously.[13] Briefly, ScanAsyst silicon nitride probes (Bruker) with nominal tip radius of 2 nm and nominal spring constant of 0.4 N/m were used. Topographical height images with a scan size of 4 × 4 μm and 2048 × 2048 pixels or 8 × 8 μm and 4096 × 4096 pixels were collected, maintaining a pixel density of 0.512 pixels/nm. A scan rate of 0.305 Hz was used for the 4 × 4 μm and 0.2 Hz for the 8 × 8 μm scans. The fibrils were probed gently using ~400 pN of peak-force, with a noise threshold setting of 0.5 nm and the Z limit was of 1.5 μm were used.

Initial image processing

Nanoscope analysis software supplied with the Multimode 8 SPM instrument (version 1.5, Bruker) were used for the initial processing of the z-height image data. Line flattening was performed to remove tilt and scanner bow by fitting a 3rd-order polynomial baseline to each scan line of the z-height channel image. For background flattening, the thresholding option in Nanoscope analysis was used and the thresholding level was manually adjusted prior to the polynomial fit. The height channel of the data was then imported into Trace_y for the subsequent steps of the workflow.

QUANTIFICATION AND STATISTICAL ANALYSIS

The algorithms in the Trace_y workflow were implemented in Matlab (2024a, The MathWorks, Natick, MA) and include graphical user-interface for various steps in the workflow that requires user inputs. Equation 1 describes the Gaussian wall model[39] used to determine a point's coordinates $\hat{x}$ and $\hat{y}$ along the central filament contour.

$$z = h\cdot\exp\left[-\frac{1}{2\sigma^2}\left((x-\hat{x})\sin\phi+(y-\hat{y})\cos\phi+c((x-\hat{x})\cos\phi+(y-\hat{y})\sin\phi)^2\right)^2\right] \quad \text{(Equation 1)}$$

In Equation 1, h is the height of the Gaussian wall, σ is the standard deviation of the Gaussian cross-section, ϕ is the angle of the filament on the x/y-plane and c is the curvature parameter. The 3D reconstruction of tip-sample contact points were performed by image deconvolution as previously described (example in Figure 3).[14] For the deconvolution procedure, a rounded cone tip model made by rotation of the half cross-section described by Equation 2 around the y-axis is used.

$$y = \begin{cases} -\sqrt{r^2-x^2}+\dfrac{r}{\sin\alpha}, & 0\le x<r\cos\alpha \\ x\cot\alpha, & x\ge r\cos\alpha \end{cases} \quad \text{(Equation 2)}$$

In Equation 2, α is the half-angle of the tip cone and was set to 18° here (estimated from the tip geometry information provided by the manufacturer). The *r* parameter is the tip-radius. The cross-section contact-point density maps (Figures 1G and 4C) was constructed using a non-parametric bivariate Normal kernel density estimator (Equation 3).

$$\widehat{f}_{\mathbf{H}}(\mathbf{x};\mathbf{H}) = \frac{1}{n}\sum_{i=1}^{n} K_{\mathbf{H}}(\mathbf{x}-\mathbf{x}_i); \quad K_{\mathbf{H}} = \frac{1}{2\pi}|\mathbf{H}|^{-1/2} e^{-\frac{1}{2}\mathbf{x}^{\mathsf{T}}\mathbf{H}^{-1}\mathbf{x}} \tag{Equation 3}$$

In Equation 3, $\widehat{f}_{\mathbf{H}}$ is the estimated contact-point density, **x** are the *x, z* coordinates vectors. $K_{\mathbf{H}}$ is the Normal kernel distribution, and **H** is the bandwidth parameter. For the bandwidth parameter, a scalar bandwidth parameter estimated with a non-parametric method[41] times the identity matrix is used. The spatial resolution for the cross-section contact-point density map were estimated using Fourier ring correlation (Equation 4) evaluated with the ½-bit information criterion (Equation 5).[40]

$$FRC_{1,2}(r_i) = \frac{\sum_{r\in r_i} F_1(r)\cdot F_2(r)^*}{\sqrt{\left(\sum_{r\in r_i}|F_1(r)|^2\right)\cdot\left(\sum_{r\in r_i}|F_2(r)|^2\right)}} \tag{Equation 4}$$

$$T_{1/2-bit}(r_i) = \frac{0.2071+1.9102\cdot\frac{1}{\sqrt{n(r_i)}}}{1.2071+0.9102\cdot\frac{1}{\sqrt{n(r_i)}}} \tag{Equation 5}$$

In Equations 4 and 5, $FRC_{1,2}$ denotes the Fourier ring correlation for each ring r_i in the Fourier space of density images 1 and 2, and n denotes the number of pixels in each ring. The Software package containing the code, and stand-alone executable of Trace_y (current version 7) prepared using Matlab Compiler (Matlab 2024a), can be downloaded from the GitHub (https://github.com/wfxue/Trace_y).